Plastic deformation via hierarchical nano-sized martensitic twinning in the metastable β Ti-24Nb-4Zr-8Sn alloy

Y. Yang, Philippe Castany, Y.L Hao, T. Gloriant

Plastic deformation via hierarchical nano-sized martensitic twinning in the metastable β Ti-24Nb-4Zr-8Sn alloy

Y. Yang[1,2], P. Castany[1,*], Y.L. Hao[3], T. Gloriant[1]

[1] Univ Rennes, INSA Rennes, CNRS, ISCR - UMR 6226, F-35000 Rennes, France

[2] School of Electromechanical Engineering, Guangdong University of Technology, Guangzhou 510006, China

[3] Institute of Metal Research, Chinese Academy of Sciences, 72 Wenhua Road, 110016 Shenyang, China

[*] Corresponding author: philippe.castany@insa-rennes.fr

Abstract

A superelastic metastable β Ti-24Nb-4Zr-8Sn (wt.%) alloy is analyzed in the solution treated state after different applied strains in order to reveal evolution of microstructures and explore plastic deformation mechanisms. Deformation bands are observed by optical microscopy, EBSD and TEM. After 3% of strain, only few thin $\{332\}\langle 113\rangle_\beta$ twins are observed, while after 5% of strain, complex hierarchically β twinning structures composed of primary and secondary bands are observed by TEM. Indeed, very thin secondary $\{332\}\langle 113\rangle_\beta$ twins are observed (about 50 nm in average) and their massive occurrence leads to the loss of the initial $\{332\}\langle 113\rangle_\beta$ twinning relationship between matrix and primary bands which is transformed passively to an unusual type II $\langle 531\rangle_\beta$ twinning relationship. Similarly, the orientation relationship between matrix and secondary twins tends to another abnormal type I $\{541\}_\beta$ twinning relationship. As *in situ* synchrotron XRD experiments show that almost all the β phase is transformed into α" martensite under loading condition, a crystallographic reconstructing method is then used to determine the real α″ orientation

before stress releasing. The relaxed {332}<113>$_{\beta}$ twins is found to correspond perfectly to the reversion of {130}<310>$_{\alpha''}$ martensitic twins occurring under loading condition. The unusual twinning relationships between matrix and primary/secondary twins are shown to correspond to type II <512>$_{\alpha''}$ and no twinning relationships in α" martensite, respectively. Schmid factor analyses show that the activation of primary twins obeys the Schmid law. However, the activation of secondary twins disobeys the Schmid law due to the variant selection of α" martensite occurring during primary twinning.

Keywords: metastable β titanium; Ti2448 alloy; plastic deformation; twinning; secondary twinning; α″ martensite.

1. Introduction

Plastic deformation is dominated mainly by dislocation movements, but can be supplemented by phase transformation and twinning, especially for steels [1-3] and β titanium alloys [4-7] known as TRIP (TRansformation Induced Plasticity) and TWIP (TWinning Induced Plasticity) effects leading to improved ductility. In the case of metastable β titanium alloys, two typical twinning modes, namely {332}<113>$_{\beta}$ and {112}<111>$_{\beta}$, were observed frequently in deformed alloys [8-18]. On the other hand, a stress-induced martensitic (SIM) transformation is observed to occur from the bcc metastable β phase to an orthorhombic C-centered α" phase [19-21]. Depending on the β phase stability, this SIM transformation can be reversible when the stress is removed, leading to superelasticity [7]. The responsibility of SIM α″ transformation for superelasticity in Ti-based alloys was well investigated in the last decade, particularly by using *in situ* techniques, like neutron diffraction [22], synchrotron X-ray diffraction [10,21,23] as well as thermo-mechanical cycling tests [24-26]. On the plastic stage, although the SIM α″ microstructures existed in some cases [7,9,27-30], observations can be limited due to the unstable nature of the SIM α″ phase which transforms back to the parent β phase easily via releasing stress. Another limiting point lies also in the spontaneous strain relaxation during the preparation of thin foils for TEM observations [31]. These bring difficulties in investigating the contribution of SIM α″ to both superelasticity and plasticity.

In the present study, a metastable β titanium alloy with a nominal composition of Ti-24Nb-4Zr-8Sn (wt.%, Ti2448 for short) is used. This alloy designed purposely for biomedical implantation and prostheses exhibits a low Young's modulus (42GPa) and superelastic behavior characterized by a maximum recoverable strain up to 3.3% [32-34]. As the origin of superelasticity, the SIM α″ transformation was definitely evidenced by *in situ* synchrotron X-ray diffraction in solution treated material [35], while this SIM transformation can be hindered in hot-forged materials [23,32,33]. However, the plastically deformed SIM α″ phase was never observed in deformed Ti2448 alloy by TEM and the mechanisms of plastic deformation, such as twinning, are difficult to investigate. In order to resolve this problem, a reconstructing method can be used [36-40] and was successfully employed in β titanium alloys according to the lattice correspondence from the β phase to α″ phase [14]. The principle of this method is based on the phenomenological theory of martensite crystallography (PTMC) [41,42]. In detail, the three principal axes of orthorhombic α″ crystal $[100]_{\alpha''}$, $[010]_{\alpha''}$, $[001]_{\alpha''}$ are derived from certain orientations of a β crystal, as following: $[100]_{\alpha''}$-$<100>_{\beta}$, $[010]_{\alpha''}$-$<01\text{-}1>_{\beta}$ and $[001]_{\alpha''}$-$<011>_{\beta}$ [43]. According to this orientation relationship (OR), six crystallographic orientations of α", named correspondence variants (CV), can be obtained from one β phase parent crystal, as illustrated in the Fig 1. These six possible variants are designated as CV1 to CV6 highlighted in color online. This method was recently used successfully to elucidate the origin of the $\{332\}<113>_{\beta}$ twinning in superelastic alloys, which was evidenced to be the resultant, during the reverse SIM transformation, of $\{130\}<310>_{\alpha''}$ twins formed in α" martensite [14]. Some transitional structures showing residual α" martensite along $\{332\}<113>_{\beta}$ twin boundaries also highlighted this mechanism of twin reversion [44,45]. Similarly, classical $\{112\}<111>_{\beta}$ twins were also shown to be the result of the reversion of $\{110\}<110>_{\alpha''}$ twins formed under stress in α" martensite of a Ti2448 single crystal [15]. These twinning systems of α" martensite was also directly evidenced in deformed shape memory full-α" alloys, for which the α" is more stable: $\{110\}<110>_{\alpha''}$ twins at the surface of specimens [28] and $\{130\}<310>_{\alpha''}$ twins in bulk materials [46,47].

Deformation twinning in superelastic titanium alloys is mostly composed of single variant twins with width reaching up to several tens of microns [8-16]. In this study, we found

a different configuration of twins in the Ti2448 alloy in the solution treated state, wherein a hierarchical β twinned structure with a sub-micron size will be shown. Indeed, all primary deformation twins contain numerous nano-sized twins of a second twin variant leading to a unique deformation microstructure in this type of alloys. The objective of the present investigation is therefore to reveal the microstructure after plastic deformation and to investigate the role of SIM α″ transformation in the Ti2448 alloy. Synchrotron X-ray diffraction and crystallographic analysis will confirm that this typical hierarchical microstructure is the result of relaxation of hierarchically twinned martensite.

2. Materials and methods

A hot-forged ingot of Ti-24Nb-4Zr-8Sn (wt. %) alloy with diameter of 55 mm was used as raw material in this work. A slice-cut sample was directly multi-pass cold rolled without intermediate annealing to the final thickness of about 0.5 mm with a cold rolling reduction rate of 94%. Then, the cold-rolled specimens were solution treated in a secondary vacuum furnace at 900 ºC for 30 minutes followed by water quenching (solution treated state, labeled as ST). After that, all specimens were cleaned in an acid solution made of 50% HF and 50% HNO_3 (vol. %) to remove any oxidation layer. The initial microstructure is thus composed of equiaxial grains of β phase with an average grain size of 50 μm [34]. Cyclic tensile tests were conducted on INSTRON 3369 tensile machine with a strain rate of 10^{-4} s^{-1}, which consist of strain increments of 0.5% followed by stress release at each cycle up to an elongation of 3% or 5%. An extensometer was used to ensure the accurate control of strain. The Young's modulus was measured from the slope of the linear part of the stress-strain curve. Phase constitution under stress was determined from *in situ* synchrotron X-ray diffraction (SXRD) during the same tensile test on the beamline ID31 of the European Synchrotron Radiation Facility (ESRF) in Grenoble, France using a 0.040002106 nm wavelength radiation (more details are available in the references [21,35]). A bank of nine detectors scanning vertically was used to measure transmitted diffracted intensities.

Optical microstructure observation was used to exhibit deformed morphology with a Leica microscope. The specimens were mechanically grinded with increasing grades of SiC

abrasive papers and then polished with a colloidal silica suspension. Finally, each specimen was etched by a solution composed of 8% HF, 15% HNO_3 and 77% H_2O (vol. %). Electron Backscattered Diffraction in Scanning Electron Microscopy (SEM-EBSD) analyses were performed in a JEOL JSM 6400 microscope equipped with a TSL-EBSD system and using an accelerating voltage of 20 kV and a step size of 0.1 µm. Samples were prepared with the same method than the optical microscopy.

Transmission electron microscopy (TEM) observations were conducted using a JEOL 2100 microscope operating at 200 kV. Thin foils for TEM were firstly mechanically cut as disks of 3 mm in diameter and polished to a thickness of 150 µm. Then, specimens were twin-jet electropolished at 253-263 K in a solution of 6% perchloric acid and 94% methanol (vol. %) and stopped before perforation. Final step of thinning was performed by two-steps ion milling using successively 5 kV and 1 keV Ar ions with a Fischione 1010 Model.

3. Results

3.1 Tensile behavior and optical microstructure

Fig. 2(a) displays the cyclic tensile curve for the ST Ti2448 alloy. Incipient Young's modulus was measured at 58GPa. A double yielding phenomenon and pseudo-elastic hysteresis loops associated with the SIM α″ transformation occurred as previously reported [34]. For microstructure observations, two samples were taken from interrupted tensile tests as indicated in Fig. 2(a): sample A after a deformation of 3% and sample B after a deformation of 5%. The Fig. 2(b) presents partial SXRD profiles of each sample taken *in situ* during the same cyclic tensile test under loading and unloading conditions [35]. Therefore, the phase composition for sample A is identified as α″+β under stress when the specimen is strained at 3% and only β phase after unloading. As previously reported, a reversible SIM transformation occurs in this alloy when a stress is applied and, after being strained up to 3%, this SIM transformation is thus totally reversible leading to superelasticity [35]. Similarly, when the strain is increased up to 5%, this alloy (sample B) mainly consists of only α″ phase under stress and α″+β after unloading. This is also supported by the vanishing of all peaks of

β phase initially present as shown in the full diffractograms available in Fig. S1 (supplementary material). Evolution of phase constitution can also be estimated from relative intensities of peaks of each phase plotted as a function of applied strain as shown on Fig. 2(c). Black circles represent the ratio of the intensity of the $\{110\}_{\beta}$ peak at each value of applied strain to its initial value and white circles represent the ratio of the intensity of the $\{020\}_{\alpha''}$ peak to its maximal value at 5% of applied strain. The decrease of volume fraction of β phase is then highlighted by the decrease of the intensity of the $\{110\}_{\beta}$ peak, which is concomitant with the increase of volume fraction of α" martensite. The β phase is thus almost totally transformed into α" when the specimen is strained at 5%, but this transformation is not totally reversible due to the onset of plasticity which hinders the reverse transformation and leads to a dual phase microstructure after releasing the stress. The SIM transformation is very dependent on thermo-mechanical process in the Ti2448 alloy: This transformation can be clearly hindered in hot-worked materials [23,32,33] while it is promoted in solution treated materials [15,34,35] as in the present study. Occurrence of an almost full transformation of β phase was also previously reported in this alloy, with a volume fraction of α" martensite measured to reach until 95% under loading [23]. The maximal measured recoverable strain (2.3% from Fig. 2(a) and [34]) is another evidence of the almost complete transformation of β phase into α" martensite. Indeed, a previous study about crystallographic texture of the present Ti2448 alloy showed that the major proportion of grains have <112> directions along the tensile direction while another minor proportion is along <110> directions [34]. The theoretical transformation strain can thus be calculated along these two directions from lattice parameters obtained by our SXRD experiments [48]: 2% along <112> and 3.1% along <110> directions. The measured value of 2.3% is then consistent with an almost complete transformation of β phase into α", otherwise this value should be much lower than 2% according to the crystallographic texture. Moreover, due to this texture and the setup configuration, the diffracted {110} and {112} peaks of β phase (Fig. 2(b) and Fig. S1) corresponds to most of the grains of the material. Consequently, when these peaks disappear, this means that these grains, i.e. most of grains of the material, are totally transformed into α" martensite.

Optical microscopy is then used to observe large areas of microstructures for sample A

and sample B deformed to different strains (Fig. 3(a) and (b), respectively). In Fig. 3(a), equiaxed grains are observed without any visible trace of SIM α″ transformation due to its complete reversibility as proved by the sole β peak in the SXRD profile in Fig. 2(b). No plasticity can thus be observed in this sample at the micron scale. However, when the applied strain increased up to 5 %, numerous deformation bands are visible in most of grains in Fig. 3(b), showing that twinning is extensively activated at this stage of deformation.

3.2 EBSD analysis

For the analysis of deformation microstructures, EBSD was employed for further identification. As deformation is shown to be similar in most of grains by optical microscopy (Fig. 3), EBSD analysis is then focused on few representative grains in order to characterize the microstructure at a finer scale. Image quality (IQ) and inverse pole figure (IPF) maps are shown in Fig. 4 for samples A and B, respectively. The IQ map constructed from electron backscattered diffraction data provides useful visualization of microstructure; its contrast arises from a variety of factors like strain, topography, phase and grain boundaries. The IPF map highlights the crystallographic orientation of each grain. For sample A, the IQ map (Fig. 4(a)) shows only grain boundaries without any deformation features inside the grains that is consistent with optical micrography (Fig. 3(a)). The corresponding IPF map of the normal direction (Fig. 4(c)) reveals a strong texture with <111> directions parallel to the normal direction, which is in accordance with the γ-fiber texture analyzed previously by XRD [34]. However, no visible martensitic phase or deformation band can be detected on either the IQ or IPF maps in sample A.

In sample B (Fig. 4(b)), deformation bands with width of 1-2 μm are strongly contrasted on the IQ map. However, these bands cannot be properly indexed whereas the matrix is perfectly indexed as β phase (Fig. 4(d)). In this alloy, deformation bands are not homogeneously indexed, contrarily to other similar metastable β titanium alloys, where {332}<113> or {112}<111> twins are unambiguously indexed with the same SEM-EBSD apparatus [9,11,49]. This comparison excludes technical settings during the indexation. Consequently, deformation bands in the present Ti2448 alloy cannot be identified as simple

twins by EBSD. In order to reveal the details of these deformation bands, TEM analyses were next performed.

3.3 TEM identification of deformation twins

Fig. 5(a) shows firstly a bright field image (BFI) obtained from the sample A deformed at 3% of strain with a nano-sized deformation band (100 nm wide) which is nearly edge-on. Fig. 5(b) shows the corresponding selected area electron diffraction (SAED) pattern captured on the boundary of the band and matrix. It is analyzed as two zone axis nearly parallel: $<111>_{matrix}$ // $<113>_{band}$. This orientation relationship between the matrix and the band corresponds to $\{332\}<113>_{\beta}$ twinning for which these two zone axis are theoretically disorientated of about 4°. This twinning relationship will be discussed in more details by the examination of stereographic projections in the section 4.1. It is also interesting to notice the high density of dislocations in the vicinity of this twin boundary which implies a strong internal stress field. Such high density of dislocations is a common feature accompanying the observation of $\{332\}<113>_{\beta}$ twins in metastable β titanium alloys [8,17,44].

The Fig. 6(a) displays the same area under another diffracting condition with the twin boundary edge-on (i.e. with the twin boundary parallel to the electron beam). The corresponding SAED pattern is shown in Fig. 6(b) and corresponds to a $<133>_{\beta}$ zone axis for each crystal misorientated of 82°. A key diagram is also provided in Fig. 6(b) with spots related to the matrix in red color and the spots related to the twin in blue color. One can also notice the presence of another set of spots with weaker intensity whose positions correspond to the ω phase as displayed in grey color in the key diagram. This ω phase is orientated along a $[-2\ -5\ 7\ -15]_{\omega}$ zone axis and some spots are due to double diffraction (white spots in the key diagram). The dark field image (DFI) of the twin in Fig. 6(d) is thus highlighted with the diffraction spot marked by blue circle in Fig. 6(b), while DFI with a less intense spot attributed to the ω phase and marked with a white circle is shown in Fig. 6(e). This figure highlights thus the presence of the ω phase thin layer located along the twin boundaries. Several samples were observed and very few similar bands were observed. It is finally worth noting that this kind of twin was not visible in optical micrographs or EBSD maps due to their

small size and very few quantities. At this stage of deformation, the microstructure is thus mainly composed of apparently undeformed β grains as shown in Fig. 3(a) and Fig. 4(a).

When the Ti2448 alloy is deformed to 5% of strain, a typical deformation microstructure is shown in Fig. 7(a), in which several bands with width of about 1 μm are visible. Some of these bands are crossing with other ones. If focused on a local part (Fig. 7(b)), these deformation bands consist of a hierarchical microstructure. Each band with 1μm in width contains numerous internal and parallel nano-sized bands with an average width smaller than 100 nm (typically 30-50 nm). It has to be noticed that all the deformation bands contain such internal secondary bands in the specimen deformed up to 5% of strain. The presence of this hierarchical nano-sized microstructure is then thought to be at the origin of the difficulty to index such deformation bands by EBSD (Fig. 4(d)). Indeed, due to the nanometric size of internal secondary bands, it is highly probable that some of the acquired Kikuchi patterns are the result of the superimposition of Kikuchi patterns of both primary and secondary internal bands, leading thus to a difficulty to correctly identify the crystallographic orientation. Moreover, the high density of boundaries inside the deformation bands also decreases the quality of indexation as shown on the IQ map (Fig. 4(b)) wherein deformation bands appear to have lower IQ values than other parts of the microstructure.

In order to distinguish different components of the complex hierarchical nano-sized deformation bands shown in Fig. 7(b), a SAED pattern of this band (Fig. 8(a)) with its key diagram (Fig. 8(b)) and several DFIs (Fig. 8(d-g)) are presented. As this SAED pattern correspond to the superimposition of diffraction patterns of the deformation band with internal bands and the surrounding matrix, a SAED pattern taken from the matrix only is also provided for a better discernibility in Fig. 8(c). This series of image is taken with all the boundaries edge-on, i.e. the boundary between both internal bands and the boundary with the surrounding grain. The SAED pattern of Fig. 8(a) reveals the existence of β phase and ω phase only rather than martensitic α″ phase. The DFIs in Fig. 8(d), Fig. 8(e), Fig. 8(f) and Fig. 8(g) are imaged with the diffraction spots marked with blue, green, red and white circles in Fig. 8(a), respectively. For an easier description, the four components in Fig. 8(d), Fig. 8(e), Fig. 8(f) and Fig. 8(g) are designated as primary band, secondary band, matrix and interfacial ω phase, respectively. A key diagram of some spots of ω phase is also presented in

Fig. 8(b) with grey color. The spots of ω phase on the SAED pattern in Fig. 8(a) are quite diffuse and elongated due to the aspect ratio of ω phase layers. As the $\{0001\}_\omega$ and $\{12\text{-}30\}_\omega$ spots can be easily distinguished because there are not superimposed with other spots of β phase, a $[\text{-}5410]_\omega$ zone axis can be determined from the diffraction pattern. Lattice parameters of ω phase are then about $a_\omega = 0.44$ nm and $c_\omega = 0.27$ nm, which are similar to a previous report of such interfacial ω phase in a Ti-27Nb alloy [14]. However, other spots of ω phase are also present and correspond to other crystallographic orientations. Indeed, as shown on the Fig. 8(g), ω phase lies along different interfaces and thus exhibit different crystallographic orientations. Nevertheless, all ω phase layers have $\{0001\}_\omega$ planes with a roughly near orientation, that is why all the interfacial ω phase can be highlighted in the DFI of Fig. 8(g).

The key diagram in Fig. 8(b) shows that the primary and secondary bands share a common $<110>_\beta$ zone axis misorientated of 50.4°, which is typical of $\{332\}<113>_\beta$ twins. This feature demonstrates unambiguously the $\{332\}<113>_\beta$ twinning relationship between primary and secondary bands. This twinning relationship was reported as the most frequent one for twins in deformed metastable β titanium alloys [8,9,11,12,29]. However, the crystallographic orientation relationships (OR) between the internal bands and the matrix are not classical. The SAED pattern of Fig. 8(a) and (c) show the matrix is orientated near a $<531>_\beta$ zone axis which is thus nearly parallel to a $<110>_\beta$ zone axis of both internal bands. The determination of this unusual OR is done from the stereographic projections of each of these three crystals, which are shown in Fig. 10 (a) to (c). Between the primary band and the matrix, the $(01\text{-}3)_\beta$ pole of the matrix is common with the $(310)_\beta$ pole of the primary band; this $\{013\}_\beta$ plane is thus common to both crystals. In addition, the trace of this common $\{013\}_\beta$ plane corresponds to the trace of the boundary between the primary band and the matrix on the TEM micrographs (Fig. 8). This common $\{013\}_\beta$ plane is then the twinning plane K1 if the OR between these two crystals is a twinning one. In the same way, the $(\text{-}531)_\beta$ pole of the matrix and the $(1\text{-}3\text{-}5)_\beta$ pole of the primary band are nearly common and are located on the trace of the common $\{013\}_\beta$ plane of both crystals. This common $<531>_\beta$ direction can then be the twinning direction η1 if a twinning OR exists between these two crystals. In order to validate a twinning OR between the matrix and the primary band, rotations of 180° around these two common poles are then performed. These operations also

allow to determine the type of the twinning OR. Thereby, a rotation of 180° around the common $\{531\}_\beta$ pole of the matrix conducts nearly to the orientation of the primary band, while a rotation of 180° around the common $\{013\}_\beta$ pole not. As a rotation of 180° around the common direction of both crystals leads to the same orientation and a rotation of 180° around the normal of the twinning plane not, this twinning relationship is then of type II and, in turn, the $\{013\}_\beta$ K1 plane has probably irrational indices. As a consequence, the exact K1 plane is only approximated by the $\{013\}_\beta$ plane. According to conventional notations, probable irrational indices are then denoted with quotation marks. This OR corresponds thus to a "{013}"$<531>_\beta$ type II twinning relationship. Similarly, $\{541\}_\beta$ and $\{111\}_\beta$ poles are nearly common between the matrix and the secondary band and a rotation of 180° around the common $\{541\}_\beta$ pole of the matrix conducts nearly to the orientation of the secondary band, while a rotation of 180° around the common $\{111\}_\beta$ pole not. The trace of the common $\{541\}_\beta$ plane corresponds also to the trace of the boundary between the secondary bands and the matrix on the TEM micrographs (Fig. 8). This twinning relationship is then of type I. The exact η1 direction is thus approximated by the $<111>_\beta$ direction and its indices are probably irrational. This OR corresponds thus to a {541}"$<111>$"$_\beta$ type I twinning relationship. These two twinning systems were predicted from calculations to be possible twinning systems in bcc metallic structures [50] and "{013}"$<531>_\beta$ twins were already observed in some bcc alloys as unusual twinning modes [50,51]. According to Christian and Mahajan [50], the other twinning elements K2 and η2 of "{013}"$<531>_\beta$ type II and {541}"$<111>$"$_\beta$ type I twinning systems are {541}"$<111>$"$_\beta$ and "{431}"$<139>_\beta$, respectively. The appearance of these abnormal twinning relationships in bcc β phase will be further explained in section 4.1.

4. Analysis and Discussion

4.1 Crystallographic reconstruction of martensitic twins under loading condition

The SIM transformation was obviously evidenced with SXRD profiles in Fig. 2(b). For the 3% of strain under loading condition (sample A), some residual β phase still remains but the microstructure is mainly composed of α" stress-induced martensite (SIM). For the sample

B deformed to 5% of strain, only SIM α" is detected under loading condition. However, only β phase and a few amount of interfacial ω phase rather than α″ phase were observed by TEM after unloading (Fig. 6 and 8). This implies that the microstructure observed by TEM corresponds to a reverse microstructure wherein all SIM α" has transformed back to β phase due to the reversibility of this transformation (Fig. 2(b)). Some remaining α" has still to be present after 5% of deformation (Fig. 2(b)) but it is also transformed back to β phase, most probably during the thinning process of TEM samples and/or by relaxation at room temperature during the storage of the specimen. Therefore, the real deformation mechanism involving the α" phase under loading condition can be reconstructed using the orientation relationship between β and α" phases as shown in Fig. 1. Based on easily known β orientations of matrix, primary and secondary bands which were determined by SAED patterns, the six possible corresponding variants (CV1 to CV6) of α″ phase for each crystal can be reconstructed. The number of each variant is labeled as defined in the Ref. [43]. It has also to be noticed that stress induced α" martensite is generally formed as un-twinned single variants in β Ti-based superelastic alloys as supported by TEM observations of residual α" martensite [9,16,27,30]. The variant really formed under loading condition can thus be deduced from the calculation of the transformation strain of each variant. Indeed, if the tensile direction is known, one can calculate the CV*i* leading to the maximum of elongation along the tensile direction [46,48,52]. It is thus assumed that this CV*i* will be formed in order to best accommodate the applied strain [46,47]. Subsequently, the real twinning relationship occurring in the SIM α″ can be found.

This method is first applied in the sample A (strained up to 3%) for the band observed in Fig. 5 and 6. The stereographic projections of the β phase crystallographic orientations of the matrix and the band are shown in Fig. 9(a) and 9(b), respectively. For a better readability, only the three $\{100\}_\beta$ poles and some other poles and traces of interest are presented. The band clearly share a common $\{332\}_\beta$ pole and a $<113>_\beta$ direction with the matrix, which highlights the well-known $\{332\}<113>_\beta$ twinning relationship. In the matrix, the tensile direction lies along $[-5\ 9\ -4]_\beta$ and allows to calculate that the CV6 leads to the maximum transformation strain (Table 1). The transformation strain of each CV is reported in Table 1 using lattice parameters of both phases obtained from synchrotron XRD experiments of the

same alloy [35]. This CV6 is thus expected to be formed during the tensile test and is reported in Fig. 9(c). For the matrix, the $(130)_{\alpha''}$ plane is thus parallel to the $\{332\}_{\beta}$ twinning plane in β phase and the $[3\text{-}10]_{\alpha''}$ direction is parallel to the $<113>_{\beta}$ twinning direction in β phase. In addition, a rotation of 180° around $(130)_{\alpha''}$ or $[3\text{-}10]_{\alpha''}$ leads to the expected orientation of the twin in α" phase (Fig. 9(d)), which also corresponds to the CV6 of the observed orientation of the β-twin. As already reported [14], the $\{332\}<113>_{\beta}$ twins observed here are due to the reversion of $\{130\}<310>_{\alpha''}$ twins really occurring in the SIM α" phase under stress. The five other CVs for both matrix and band were also constructed to verify that no other potential twinning relationship in α" exist.

The same procedure is then applied for the sample B (deformed at 5% of strain) in order to analyze the complex hierarchically β-twinned microstructure of Fig. 8. The crystallographic orientations of β-matrix, β-primary band and β-secondary band obtained from SAED patterns, are represented by stereographic projections in Fig. 10(a), 10(b) and 10(c), respectively. It is demonstrated clearly that the β-primary band and the β-secondary band keep a $\{332\}<113>_{\beta}$ twinning relationship, because the two projections share a common $\{332\}_{\beta}$ pole and a common $<113>_{\beta}$ direction indicated in Fig. 10(b) and 10(c). Indeed, the operation of a reflection on the $(332)_{\beta}$ plane or a rotation of 180^{o} around the $[\text{-}1\text{-}13]_{\beta}$ direction of the β-primary band leads to the orientation of the β-secondary band. Therefore, the β-primary band and β-secondary band are perfectly in the $\{332\}<113>$ twinning relationship.

Then, the stereographic projections of the corresponding α″ phase are reconstructed. The six possible α″-variants (CV1-CV6) are deduced from either β-primary band or β-secondary band orientations. The sole convincing possibility is represented in Fig. 10(e) and 10(f) for α″-primary band-CV5 and α″-secondary band-CV5 that corresponds to a compound $\{130\}<310>_{\alpha''}$ twin. As for the sample A, the twining plane $(130)_{\alpha''}$ and the twining direction $[3\text{-}10]_{\alpha''}$ indicated in Fig. 10(e) coincide with the twining plane $(332)_{\beta}$ and the twining direction $[\text{-}1\text{-}13]_{\beta}$ in Fig. 10(b), respectively, indicating a clear correspondence between the deduced $\{130\}<310>_{\alpha''}$ twinning system in the α" phase and the observed twinning system in the relaxed β phase. Although twinning in α" martensite was not deeply investigated in Ti-based alloys, occurrence of this $\{130\}<310>_{\alpha''}$ twinning system in α" martensite was

recently proved for the first time in deformed Ti-25Ta-20Nb shape memory alloy [46] and also later in stress-induced α" single crystals [47]. The correspondence between {130}<310>$_{\alpha''}$ twins and {332}<113>$_{\beta}$ twins was also evidenced in previous reports [14,46]. As a conclusion, the secondary bands referring to primary band observed as {332}<113>$_{\beta}$ twins under unloading condition were {130}<310>$_{\alpha''}$ twins under loading condition.

In terms of the orientation relationships between the matrix and primary/secondary bands in sample B, the situation is more unprecedented. It can firstly be identified a type II <531>$_{\beta}$ twinning relationship with a {013}$_{\beta}$ twinning plane (Fig. 10(a) and 10(b)) between the matrix and the primary band. By using the same method than previously, this twinning relationship corresponds to a type II <512>$_{\alpha''}$ twin in α" martensite with a {021}$_{\alpha''}$ twinning plane (Fig. 10(d) and 10(e)). Indeed, the operation of reflection on the twinning planes (01-3)$_{\beta}$ in Fig. 10(a) and (0-21)$_{\alpha''}$ in Fig 10(d) doesn't lead to the orientation of primary band but the rotation of 180° around the twinning direction [-531]$_{\beta}$ in Fig. 10(a) and [-5-1-2]$_{\alpha''}$ in Fig 10(d) does, that is why this twinning relationship is a type II one. This unusual twinning relationship was predicted from calculations in a tetragonal structure very close to the orthorhombic one of α" martensite [53], confirming the validity of our reconstruction method. Similarly, the orientation relationship between the matrix and the secondary band can be shown to be close to a type I {541}$_{\beta}$ twinning relationship with a <111>$_{\beta}$ twinning direction (Fig. 10(a) and 10(c)). However, this OR does not correspond to a twinning relationship in α" phase as the common poles in β phase do not correspond to the same type of poles in α" phase. Indeed, the {541}$_{\beta}$ apparent twinning plane corresponds to a {332}$_{\alpha''}$ type pole for the matrix (Fig. 10 d)) and to a {323}$_{\alpha''}$ pole for the secondary bands (Fig. 10(e)). The same observation can be also made for the twinning direction. It has to be noted that these unusual twinning relationships do not correspond to really activated twinning systems. Indeed, the sample A, deformed at 3% of strain, only exhibits {332}<113>$_{\beta}$ twins without secondary internal twinning. This proves that the observation of these abnormal twinning relationships is due to the loss of the initial twinning relationship due to secondary twinning activation. This point will also be discussed in the further section with regard to Schmid factor analyses. As stated in other investigations reporting secondary twinning in Mg alloys [54,55] and steels [56], secondary twins cannot

occur inside a primary twin without changing the stress state of the primary twin. The consequence is a strong distortion of the initial habit plane of the primary twin, which leads to a loss of the initial twinning relationship between the primary twin and the matrix. That is exactly the reason why the crystallographic twinning relationship between the matrix and primary band is abnormal for the sample B strained up to 5% of strain: The initial $\{332\}<113>_{\beta}$ twinning relationship between the matrix and the primary twin is lost due to massive secondary twinning inside. However, the resulting orientation relationships between the matrix and primary/secondary bands are not random and tend to adopt a configuration that minimizes the energy of the boundary. Indeed, as already mentioned in the section 3.3, the two abnormal OR presently reported are possible twinning systems in bcc structures, which were predicted from calculations [51]. The width and the frequency of secondary twins inside primary twins are thus "adjusted" to create this kind of abnormal twin boundary instead of a random OR in order to minimize the energy of the boundary between the matrix and the hierarchically twinned band.

4.2 Schmid factor analysis

As a mode of plastic deformation, the activation of a specific variant of deformation twins generally obeys the Schmid law such as in hcp Mg [57,58] and α-Ti [59,60]. In metastable β titanium alloys, Bertrand et al. first showed that the activation of $\{332\}<113>_{\beta}$ twin variants also obeys the Schmid law [11] that was further confirmed in other studies [13,61,62]. Then, the Schmid law dependence of all the twins observed in the present study will be analyzed hereafter.

The Schmid Factor (SF) is expressed as $SF = \cos\lambda \cdot \cos\varphi$, where λ is the angle between the tensile direction and the normal direction of the twinning plane K_1, and φ is the angle between the tensile direction and the twinning direction η_1. As values of λ and φ angles are both between 0^o and 180^o, the values of SF lie between -0.5 and 0.5, with positive values indicating an elongation of the crystal and negative values a compression of the crystal along the stress direction [11,50].

Schmid Factor analysis is firstly used for the sample A regarding the activation of

{332}<113>$_{\beta}$ twins in β phase, which exist under unloading condition, and then the {130}<310>$_{\alpha''}$ twin in α'' phase under loading condition. The tensile direction in the coordinate system of the β-matrix is [-59-4]$_{\beta}$ pointed out in Fig. 9(a) and the calculated SF values for all twelve variants are shown in Table 2. The effectively observed variant is the one with the highest SF value (V7 in bold in Table 2). Based on the crystallographic reconstruction for martensitic phase on loading (Fig. 9(c)), the tensile direction in the α'' phase is [-58-2]$_{\alpha''}$ and the activated (130)[-310]$_{\alpha''}$ twin has also the highest SF value (V1 in bold in Table 2). As previously reported [46], the prediction of activated twin variants by SF calculation in the β phase is equivalent to using SF calculation in the SIM α'' variant leading to the maximum of transformation strain. Indeed, in the present example, we deduced from crystallographic reconstruction (section 4.1) that the CV6 was formed in the matrix during deformation, which is really the CV giving the maximum of strain (Table 1).

The same calculation is made for the activation of secondary bands in sample B as shown in Table 2. Contrarily to sample A, the activation of secondary {332}<113>$_{\beta}$ twins does not obey the Schmid law as the activated variant (V1 in bold in Table 2) has a SF value of 0.21 while 3 other variants have similar (0.21 for V6 and 0.28 for V11) or higher values (0.46 for V8). However, regarding the α'' phase, the activation of {130}<310>$_{\alpha''}$ secondary twins obeys the Schmid law because the activated variant is the one with the highest SF value (0.20 in bold in Table 2). This result can be explained by the CV of the α'' formed during deformation. Indeed, the CV which would give the maximum of elongation for the primary band is the CV4 (last column of Table 1, value of 4.81 %) while the one observed is the CV5. But the actual CV of the primary band is due to {130}<310>$_{\alpha''}$ twinning of the matrix and not due to a direct transformation from the β phase. That is why a non-optimal variant is formed and, in turn, a non-obedience of the Schmid law appears if the β phase is considered. However, the Schmid law is followed only if α'' martensite is considered. In other words, the activation of primary twins changes the CV of martensite from CV2 to CV5 inside primary twins and, in turn, changes the crystallographic orientation of the tensile direction. The orientation of this CV2 is then favorable to activation of secondary {130}<310>$_{\alpha''}$ twins, while other CVs can be unfavorable to secondary twinning, leading to compression twins only or to SF values near to zero.

Consider now the activation of the primary band inside the matrix of the sample B. The SF calculation shows that the variant V12 (in bold in Table 2) has the highest SF value in β phase and corresponds to the highest SF value in α" too. However, it is not possible to verify directly if this twin is the activated one because the original OR is lost due to occurrence of secondary twinning. But the analysis of the trace of the twinning plane can solve the problem. In the stereographic projection of the matrix (Fig. 10(a)), the twin plane $(23\text{-}3)_{\beta}$ of the variant V12 is reported as well as the surface plane of the sample $(\text{-}4\text{-}3\text{-}3)_{\beta}$. It is thus worth noting that the trace of this twin plane is consistent with the real orientation of this plane in Fig. 8. In addition, this trace is also exactly superimposed with the trace of the abnormal twin plane $(01\text{-}3)_{\beta}$ actually observed between the matrix and the primary band. This interesting result shows that even if the activation of secondary twinning leads to the loss of the initial OR between the matrix and the primary twin, the geometrical orientation of the twinning plane remains the same while only its crystallographic features change. The activation of the primary twin is thus here similar to the sample A and obeys the Schmid law.

As a summary, the activation of primary twins strictly obeys the Schmid law, while a non-obedience can be thought to occur for secondary twinning if only the β phase is considered. However, the activation of secondary twins also obeys the Schmid law if the SIM α" phase is considered. Indeed, the Schmid law obedience for the primary twin in the β phase is due to the variant selection of martensite occurring during the tensile test. However, as this variant selection does not occur before the activation of secondary twinning inside primary twins, an apparent non-obedience of the Schmid law in the β phase can be observed.

4.3 Sequence of plastic deformation

The sequence of twinning mechanisms occurring during plastic deformation can be described according to the schematic illustration in Fig. 11. For the solution treated Ti-24Nb-4Zr-8Sn alloy, the initial recrystallized microstructure is composed of homogeneous equiaxed grains. When a tensile test is performed, several mechanisms of deformation are progressively activated as detailed hereafter:

- When the applied stress exceeds the critical stress, the SIM transformation occurs first.

This mechanism stops when each grain of β phase is transformed into one single variant (CV) of α" martensite. If the stress is released during this stage, the reversibility of this SIM transformation leads to the total recovery of the initial β microstructure.

- When the strain reaches 3%, the grains are supposed to be mainly composed of a single variant of α" martensite matrix (see SXRD results) and {130}<310>$_{\alpha''}$ twins starts to nucleate. These twins are few and very thin (about 100nm in width) at this stage (Fig. 11(a)). Once the applied stress is released (Fig. 11(c)), all the α" martensite transforms back to β phase and these {130}<310>$_{\alpha''}$ martensitic twins reverse back to {332}<113>$_{\beta}$ twins. The appearance of a thin layer of ω phase lying along the β twin boundary as well as a high density of dislocations around the β twin boundary accompany this reverse transformation. This microstructure corresponds thus to the one observed in Fig. 5 and 6.

- When the applied strain continues to increase up to 5 % strain, the quantity and width of primary twins increase (Fig. 11(b)) concomitantly with the occurrence of massive secondary twinning inside. Secondary twinning occurs with the same {130}<310>$_{\alpha''}$ martensitic twinning system than primary twinning. Secondary twins are numerous and very thin (about 50 nm in average) leading to the formation of hierarchical nano-sized deformation bands. As a consequence, the initial {130}<310>$_{\alpha''}$ twinning relationship between the primary twin and the matrix is lost. Therefore, the resulting OR between matrix and primary twins tends to a new type II <512>$_{\alpha''}$ twinning relationship. When the applied stress is totally released, the martensitic α″ phase reverses back to β phase completely as shown in Fig. 11(d). The OR between primary and secondary bands results in the classical {332}<113>$_{\beta}$ twinning relationship, while the OR between the matrix and primary twins changes passively to a type II <531>$_{\beta}$ twinning relationship. Even if no twinning relationship can be determined between matrix and secondary bands into α" phase, this OR is not random and becomes a type I {541}$_{\beta}$ twinning relationship in β phase.

Moreover, the reversion of parent martensitic twins formed in α" phase to the observed twins in β phase are all accompanied by the formation of a thin layer of ω phase along the twin boundaries (Fig. 6(e) and 8(g)). This phenomenon is attributed to strong strain relaxation occurring around twin boundaries during the reverse phase transformation. Such interfacial ω phase was already reported along twin boundaries [14,15], but the mechanism of strain

relaxation around {332}<113>$_\beta$ twins can be different depending on alloy compositions. A high density of dislocations located around the twin boundaries is then the most observed consequence of such strain relaxation [8,17,44]. In the present case, both interfacial ω phase and high density of dislocations are observed along twin boundaries (Fig. 6).

It is also worth noting that, even if primary and secondary twins are extensively activated during plastic deformation, conventional dislocation slip also occurs. As visible on Fig. 7, dislocations are present in the grains of the sample deformed to 5% of strain. However, dislocations are very few in the sample deformed to 3% of strain (Figs. 5 and 6), indicating that the critical stress to induce dislocation slip is probably not reached. Dislocation slip is thus also an operative deformation mechanism during the plastic deformation stage.

Finally, such massive secondary twinning was few reported in metastable β titanium alloys, in which twins are typically larger than in the present study (5 to 20 µm in width) and without secondary twinning [8,9,11,14,16,49]. Complex bands with secondary twins and SIM α" are however frequently observed in more stable alloys such the ones exhibiting TRIP/TWIP effects [6,7,62]. Similar secondary twinning than in the present Ti2448 was only reported in more stable Ti-Mo-V alloys [17]. The exact cause of massive secondary twinning is not known, but in some alloys, like the present Ti2448 alloy, the nucleation of secondary twins is energetically more favorable than the growth of primary twins. The reason of such phenomenon can be multiple such as precipitates or dislocations. In the present Ti2448 alloy, a high density of dislocations nucleating at the twin boundaries and thus hindering their growth could be a possible explanation. This possibility can be supported by the high density of dislocations visible around twin boundaries (Figs. 5 to 7). These dislocations are supposed to be nucleated during the reverse α"-β phase transformation and can be accumulated during the cyclic tensile test. However, such high densities of dislocations were also reported in other alloys exhibiting only large primary twins without any secondary twin [8, 14]. The exact reason of occurrence of massive secondary twinning is then probably more complex and needs further investigations to be clearly understood. Nevertheless, in the present Ti2448 alloy, over a certain width of primary twins, the critical stress to nucleate secondary twins becomes lower than the stress necessary to coarsen primary twins. This is also supported by the very thin width of secondary twins (about 50 nm) and their density: It is energetically

easier to form numerous nano-sized secondary twins instead of thickening the already nucleated ones. This feature leads then to the formation of hierarchical nano-sized twinning structures as a main mechanism of plastic deformation in the present Ti2448 alloy.

5. Conclusions

In this study, the deformation microstructures of solution treated Ti2448 alloy were investigated and the plastic deformation mechanisms were discussed. The following conclusions can be made:

(1) The ST Ti2448 alloy shows superelasticity resulting from stress-induced martensitic α'' transformation, which reverses back to β phase after releasing stress, even at the plastic deformation stage.

(2) At the early stage of plastic deformation, a few amount of primary bands, identified to be $\{332\}\langle 113\rangle_{\beta}$ twins, appeared in the deformation microstructure under unloading condition. While plastic deformation increases, complex hierarchical nano-sized deformation bands composed of primary bands with internal secondary bands were observed. Secondary bands were revealed to be $\{332\}\langle 113\rangle_{\beta}$ twins inside primary bands under unloading condition. All twin boundaries are accompanied by a thin layer of interfacial ω phase whatever the value of applied strain.

(3) The occurrence of massive secondary twinning leads to the loss of the initial $\{332\}\langle 113\rangle_{\beta}$ twinning relationship between matrix and primary twins and an unusual type II $\langle 531\rangle_{\beta}$ twinning relationship is passively formed between matrix and primary twins. The orientation relationship between matrix and secondary twins is also not random and tends to an another abnormal type I $\{541\}_{\beta}$ twinning relationship.

(4) From crystallographic reconstruction, the real α" phase orientation existing under loading condition was used to determine the effective twinning system in SIM α" phase. Occurrence of compound $\{130\}\langle 310\rangle_{\alpha''}$ twinning was thus confirmed to be the activated mechanism of deformation under loading condition. The observation of $\{332\}\langle 113\rangle_{\beta}$ twins was proved to be the result of reversibility of $\{130\}\langle 310\rangle_{\alpha''}$ twins in α" martensite. The orientation relationship between matrix and primary twins is shown to be type II $\langle 512\rangle_{\alpha''}$

while no twinning relationship between matrix and secondary twins can be found in α" martensite.

(5) Schmid law was used to predict successfully the activated twinning variant in both β and α″ phases for primary twins. However, there is a disobedience of the Schmid law for secondary twinning regarding the β phase, but not for the α" phase. This result can be explained by the variant selection of martensite due to primary twinning.

(6) Hierarchal martensitic twinning is finally revealed to be a main mechanism (complementing conventional dislocation slip) for the plastic deformation of the ST Ti2448 alloy.

Declaration of Competing Interest

The authors declare that they have no known competing financial interests or personal relationships that could have appeared to influence the work reported in this paper.

Acknowledgements

This work was financially supported by the Project supported by the National Science Foundation for Young Scientists of China (Grant No. 51801199). The authors acknowledge the THEMIS platform of the University of Rennes for providing access to TEM facilities as well as the CMEBA platform for SEM-EBSD facilities. The authors also acknowledge the European Synchrotron Radiation Facility for provision of synchrotron radiation facilities and would like to thank Yves Watier for assistance in using the beamline ID31 (actually ID22).

References

[1] H. Idrissi, K. Renard, L. Ryelandt, D. Schryvers, P.J. Jacques, On the mechanism of twin formation in Fe–Mn–C TWIP steels, Acta Mater. 58 (2010) 2464-2476.

[2] O. Grässel, L. Kruger, G. Frommeyer, L.W. Meyer, High strength Fe-Mn-(Al, Si) TRIP/TWIP steels development-propertie -application Int. J. Plasticity 16 (2000) 1391-1409.

[3] O. Bouaziz, S. Allain, C.P. Scott, P. Cugy, D. Barbier, High manganese austenitic twinning induced plasticity steels: A review of the microstructure properties relationships, Curr. Opin. Solid State. Mater. Sci. 15 (2011) 141-168.

[4] F. Sun, J.Y. Zhang, M. Marteleur, C. Brozek, E.F. Rauch, M. Veron, P. Vermaut, P.J. Jacques, F. Prima, A new titanium alloy with a combination of high strength, high strain hardening and improved ductility , Scripta Mater. 94 (2015) 17-20.

[5] M. Marteleur, F. Sun, T. Gloriant, P. Vermaut, P.J. Jacques, F. Prima, On the design of new β-metastable titanium alloys with improved work hardening rate thanks to simultaneous TRIP and TWIP effects, Scripta Mater. 66 (2012) 749-752.

[6] F. Sun, J.Y. Zhang, M. Marteleur, T. Gloriant, P. Vermaut, D. Laillé, P. Castany, C. Curfs, P.J. Jacques, F. Prima, Investigation of early stage deformation mechanisms in a metastable β titanium alloy showing combined twinning-induced plasticity and transformation-induced plasticity effects, Acta Mater. 61 (2013) 6406-6417.

[7] P. Castany, T. Gloriant, F. Sun, F. Prima, Design of strain-transformable titanium alloys, Comptes Rendus Physique 19 (2018) 710-720.

[8] S. Hanada, O. Izumi, Transmission electron microscopic observations of mechanical twinning in metastable beta titanium alloys, Metall. Trans. A 17 (1986) 1409-1420.

[9] A. Ramarolahy, P. Castany, F. Prima, P. Laheurte, I. Péron, T. Gloriant, Microstructure and mechanical behavior of superelastic Ti-24Nb-0.5O and Ti-24Nb-0.5N biomedical alloys, J. Mech. Behav. Biomed. Mater. 9 (2012) 83-90.

[10] R.J. Talling, R.J. Dashwood, M. Jackson, D. Dye, On the mechanism of superelasticity in Gum metal, Acta Mater. 57 (2009) 1188-1198.

[11] E. Bertrand, P. Castany, I. Peron, T. Gloriant, Twinning system selection in a metastable β-titanium alloy by Schmid factor analysis , Scripta Mater. 64 (2011) 1110-1113.

[12] M. Oka, Y. Taniguchi, {332} deformation twins in a Ti-15.5 pct V alloy, Metall. Trans. A 10A (1979) 651-653.

[13] X.H. Min, K. Tsuzaki, S. Emura, T. Sawaguchi, S. Li, K. Tsuchiya, {332}<113> twinning system selection in a β-type Ti-15Mo-5Zr polycrystalline alloy, Mater. Sci. Eng. A 579 (2013) 164-169.

[14] P. Castany, Y. Yang, E. Bertrand, T. Gloriant, Reversion of a parent {130}<310>$_{\alpha''}$ martensitic twinning system at the origin of {332}<113>$_{\beta}$ twins observed in metastable β titanium alloys, Phys.

Rev. Lett. 117 (2016) 245501.

[15] Y. Yang, P. Castany, E. Bertrand, M. Cornen, J.X. Lin, T. Gloriant, Stress release-induced interfacial twin boundary ω phase formation in a β type Ti-based single crystal displaying stress-induced α" martensitic transformation, Acta Mater. 149 (2018) 97-107.

[16] P. Castany, D.M. Gordin, S.I. Drob, C. Vasilescu, V. Mitran, A. Cimpean, T. Gloriant, Deformation mechanisms and biocompatibility of the superelastic Ti–23Nb–0.7Ta–2Zr–0.5N alloy, Shape Memory and Superelasticity 2 (2016) 18-28.

[17] G. Rusakov, A. Litvinov, V. Litvinov, Deformation twinning of titanium β-alloys of transition class, Met. Sci. Heat Treat. 48 (2006) 244-251.

[18] M. Ahmed, D. Wexler, G. Casillas, O.M. Ivasishin, E.V. Pereloma, The influence of β phase stability on deformation mode and compressive mechanical properties of Ti–10V–3Fe–3Al alloy, Acta Mater. 84 (2015) 124-135.

[19] M. Tahara, H.Y. Kim, H. Hosoda, S. Miyazaki, Cyclic deformation behavior of a Ti–26 at.% Nb alloy, Acta Mater. 57 (2009) 2461-2469.

[20] Y. Al-Zain, H.Y. Kim, T. Koyano, H. Hosoda, T.H. Nam, S. Miyazaki, Anomalous temperature dependence of the superelastic behavior of Ti-Nb-Mo alloys, Acta Mater. 59 (2011) 1464-1473.

[21] P. Castany, A. Ramarolahy, F. Prima, P. Laheurte, C. Curfs, T. Gloriant, In situ synchrotron X-ray diffraction study of the martensitic transformation in superelastic Ti-24Nb-0.5N and Ti-24Nb-0.5O alloys, Acta Mater. 88 (2015) 102-111.

[22] S.D. Prokoshkin, A.V. Korotitskiy, A.V. Tamonov, I.Yu. Khmelevskaya, V. Brailovski, S. Turenned, Comparative X-ray and time-of-flight neutron diffraction studies of martensite crystal lattice in stressed and unstressed binary Ti-Ni alloys, Mater. Sci. Eng. A 438-440 (2006) 549-552.

[23] E.G. Obbard, Y.L. Hao, R.J. Talling, S.J. Li, Y.W. Zhang, D. Dye, R. Yang, The effect of oxygen on α'' martensite and superelasticity in Ti-24Nb-4Zr-8Sn, Acta Mater. 59 (2011) 112-125.

[24] E. Bertrand, P. Castany, T. Gloriant, Investigation of the martensitic transformation and the damping behavior of a superelastic Ti–Ta–Nb alloyActa Mater. 61 (2013) 511-518.

[25] T. Inamura, Y. Yamamoto, H. Hosoda, H.Y. Kim, S. Miyazaki, Crystallographic orientation and stress-amplitude dependence of damping in the martensite phase in textured Ti-Nb-Al shape memory alloy, Acta Mater. 58 (2010) 2535-2544.

[26] P.J.S. Buenconsejo, H.Y. Kim, H. Hosoda, S. Miyazaki, Shape memory behavior of Ti-Ta and its

potential as a high-temperature shape memory alloy, Acta Mater. 57 (2009) 1068-1077.

[27] L.Q. Wang, W.J. Lu, J.N. Qin, F. Zhang, D. Zhang, Microstructure and mechanical properties of cold-rolled TiNbTaZr biomedical β titanium alloy, Mater. Sci. Eng. A 490 (2008) 421-426.

[28] D.H. Ping, Y. Yamabe-Mitarai, C.Y. Cui, F.X. Yin, M.A. Choudhry, Stress-induced α″ martensitic (110) twinning in β-Ti alloys, Appl. Phys. Lett. 93 (2008) 151911.

[29] F. Sun, Y.L. Hao, S. Nowak, T. Gloriant, P. Laheurte, F. Prima, A thermo-mechanical treatment to improve the superelastic performances of biomedical Ti-26Nb and Ti-20Nb-6Zr (at.%) alloys, J. Mech. Behav. Biomed. Mater. 4 (2011) 1864-1872.

[30] J.Y. Zhang, Fan S., Y.L. Hao, N. Gozdecki, E. Lebrun, P. Vermaut, R. Portier, T. Gloriant, P. Laheurte, F. Prima, Influence of equiatomic Zr/Nb substitution on superelastic behavior of Ti-Nb-Zr alloy Mater. Sci. Eng. A, 563 (2013) 78-85.

[31] G. Lütjering, J.C. Williams, Titanium. (2nd ed.) Springer-Verlag, Berlin (2007) 141.

[32] Y.L. Hao, S.J. Li, B.B. Sun, M.L. Sui, R. Yang, Ductile titanium alloy with low poisson's ratio, Phys. Rev. Lett. 98 (2007) 216405.

[33] Y.L. Hao, S.J. Li, S.Y. Sun, C.Y. Zheng, Q.M. Hu, R. Yang, Super-elastic titanium alloy with unstable plastic deformation, Appl. Phys. Lett. 87 (2005) 091906.

[34] Y. Yang, P. Castany, M. Cornen, I. Thibon, F. Prima, T. Gloriant, Texture investigation of the superelastic Ti-24Nb-4Zr-8Sn alloy, J. Alloys. Compd. 591 (2014) 85-90.

[35] Y. Yang, P. Castany, M. Cornen, F. Prima, S.J. Li, Y.L. Hao, T. Gloriant, Characterization of the martensitic transformation in the superelastic Ti-24Nb-4Zr-8Sn alloy by in situ synchrotron X-ray diffraction and dynamic mechanical analysis, Acta Mater. 88 (2015) 25-33.

[36] E. Bertrand, P. Castany, T. Gloriant, An alternative way to orient the parent phase in the cubic/orthorhombic martensitic transformation of titanium shape memory alloys, Scripta Mater. 83 (2014) 41-44.

[37] M. Humbert, F. Wagner, H. Moustahfid, C. Esling, Determination of the orientation of a parent β grain from the orientations of the inherited α plates in the phase transformation from body-centred cubic to hexagonal close packed, J. Appl. Crystallogr. 28 (1995) 571-576.

[38] M.G. Glavicic, P.A. Kobryn, T.R. Bieler, S.L. Semiatin, An automated method to determine the orientation of the high-temperature beta phase from measured EBSD data for the low-temperature alpha-phase in Ti–6Al–4V, Mater. Sci. Eng., A 351 (2003) 258-264.

[39] G. Miyamoto, N. Iwata, N. Takayama, T. Furuhara, Mapping the parent austenite orientation reconstructed from the orientation of martensite by EBSD and its application to ausformed martensite, Acta Mater. 58 (2010) 6393-6403.

[40] L. Germain, N. Gey, R. Mercier, P. Blaineau, M. Humbert, An advanced approach to reconstructing parent orientation maps in the case of approximate orientation relations: Application to steels, Acta Mater. 60 (2012) 4551-4562.

[41] C.M. Wayman, The phenomenological theory of martensite crystallography: interrelationships, Metall. Mater. Trans. A 25 (1994) 1787-1795.

[42] D.S. Lieberman, M.S. Wechsler, T.A. Read, Cubic to Orthorhombic diffusionless phase change-experimental and theoretical studies of AuCd, J. Appl. Phys. 26 (1955) 473-484.

[43] Y.W. Chai, H.Y. Kim, H. Hosoda, S. Miyazaki, Self-accommodation in Ti-Nb shape memory alloys, Acta Mater. 57 (2009), 4054-4064.

[44] M.J. Lai, C.C. Tasan, D. Raabe, On the mechanism of {332} twinning in metastable β titanium alloys, Acta Mater. 111 (2016) 173-186.

[45] B. Chen, W. Sun, Transitional structure of {332}<113> β twin boundary in a deformed metastable β-type Ti-Nb-based alloy, revealed by atomic resolution electron microscopy, Scripta Mater. 150 (2018) 115-119.

[46] E. Bertrand, P. Castany, Y. Yang, E. Menou, T. Gloriant, Deformation twinning in the full-α" martensitic Ti-25Ta-20Nb shape memory alloy, Acta Mater. 105 (2016) 94-103.

[47] M. Tahara, N. Okano, T. Inamura, H. Hosoda, Plastic deformation behaviour of single-crystalline martensite of Ti-Nb shape memory alloy, Sci. Rep. 7 (2017) 15715.

[48] H. Jabir, A. Fillon, P. Castany, T. Gloriant, Cristallographic orientation dependence of mechanical properties in the superelastic Ti-24Nb-4Zr-8Sn, Phys. Rev. Mater. 3 (2019) 063608.

[49] M. Besse, P. Castany, T. Gloriant, Mechanisms of deformation in gum metal TNTZ-O and TNTZ titanium alloys: A comparative study on the oxygen influence, Acta Mater. 59 (2011) 5982-5988.

[50] J.W. Christian, S. Mahajan, Deformation twinning, Prog. Mater. Sci. 39 (1995) 1-157.

[51] R.H. Richman, The diversity of twinning in body-centered cubic structures, in Deformation twinning, Gordon and Breach Science publishers, 1964.

[52] H.Y. Kim, Y. Ikehara, J.I. Kim, H. Hosoda, S. Miyazaki, Martensitic transformation, shape memory effect and superelasticity of Ti-Nb binary alloys, Acta Mater. 54 (2006) 2419-2429.

[53] H. Tobe, H.Y. Kim, T. Inamura, H. Hosoda, S. Miyazaki, Origin of {332} twinning in metastable β-Ti alloys, Acta Mater. 64 (2014) 345-355.

[54] É. Martin, L. Capolungo, L. Jiang, J.J. Jonas, Variant selection during secondary twinning in Mg-3%Al, Acta Mater. 58 (2010) 3970-3983.

[55] Q. Yu, J. Wang, Y. Jiang, R.J. McCabe, N. Li, C. N. Tomé, Twin–twin interactions in magnesium, Acta Mater. 77 (2014) 28-42.

[56] P. Müllner, A.E. Romanov, Internal twinning in deformation twinning, Acta Mater. 48 (2000) 2323-2337.

[57] J.J. Jonas, S. Mu, T. Al-Samman, G. Gottstein, L. Jiang, Ė. Martin, The role of strain accommodation during the variant selection of primary twins in magnesium, Acta Mater. 59 (2011) 2046-2056.

[58] S. Mu, J.J. Jonas, G. Gottstein, Variant selection of primary selection of primary, secondary and tertiary twins in a deformed Mg alloy, Acta Mater. 60 (2012) 2043-2053.

[59] L. Bao, Y. Zhang, C. Schuman, J.S. Lecomte, M.J. Philippe, X. Zhao, C. Esling, Multiple twinning in pure hexagonal close-packed titanium, J. Appl. Cryst. 46 (2013) 1397-1406.

[60] N. Bozzolo, L. Chan, A.D. Rollett, Misorientations induced by deformation twining in titanium, J. Appl. Cryst. 43 (2010) 596-602.

[61] X. Zhou, X. Min, S. Emura, K. Tsuchiya, Accommodative {332}<113>primary and secondary twinning in a slightly deformed β-type Ti-Mo titanium alloy, Mater. Sci. Eng. A 684 (2017) 456-465.

[62] L. Lilensten, Y. Danard, C. Brozek, S. Mantri, P. Castany, T. Gloriant, P. Vermaut, F. Sun, R. Banerjee, F. Prima, On the heterogeneous nature of deformation in a strain-transformable beta metastable Ti-V-Cr-Al alloy, Acta Mater. 162 (2019) 268-276.

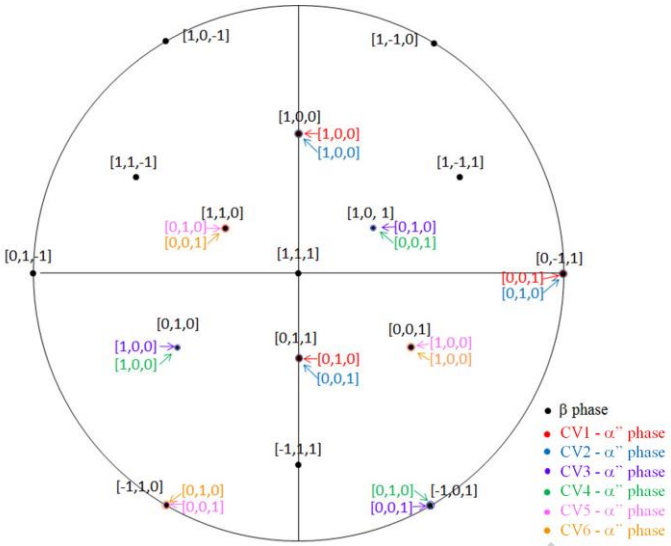

Fig. 1. Crystallographic representation of the six α″ correspondence variants (CV) according to the orientation relationship with a known β phase orientation.

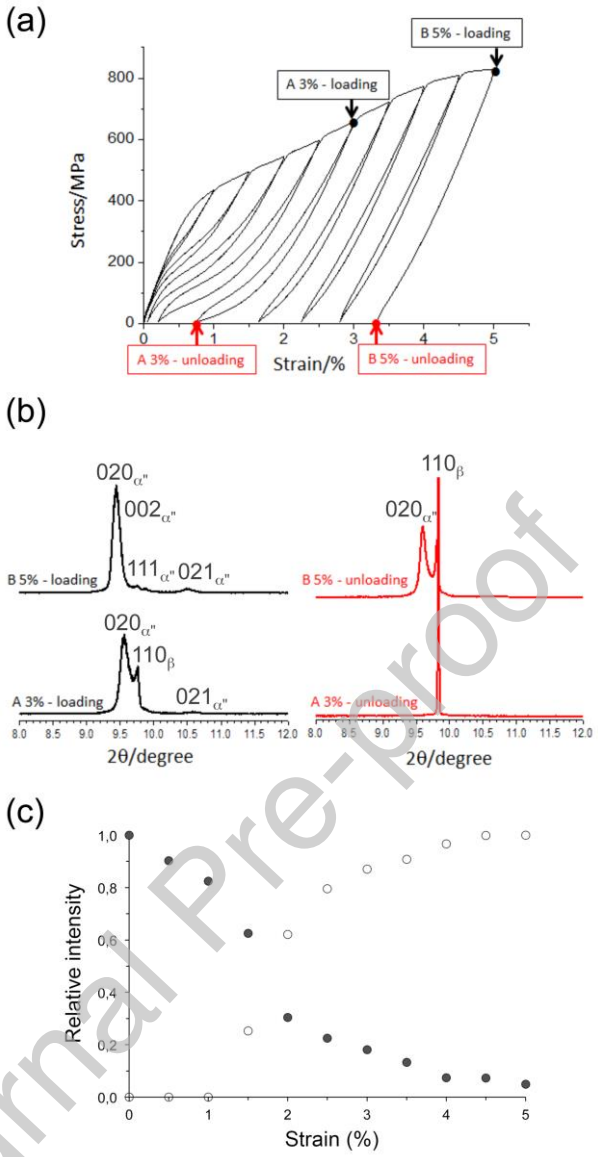

Fig. 2. (a) Cyclic tensile curve of solution treated Ti2448 alloy with the two samples taken from interrupted tests: A after 3% of strain and B after 5% of strain; (b) Phase composition under loading and after unloading conditions for each sample from *in situ* synchrotron X-ray diffraction experiments; (c) Relative intensities of 110_{β} peak (black circles) and $020_{\alpha"}$ peak (white circles) under loading condition as a function of applied strain.

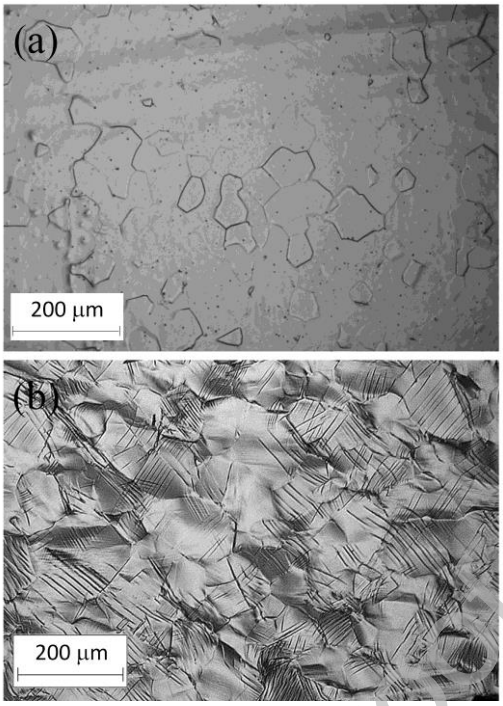

Fig. 3. Optical micrographs after deformation of (a) sample A and (b) sample B; the tensile direction lies along the horizontal direction of both micrographs.

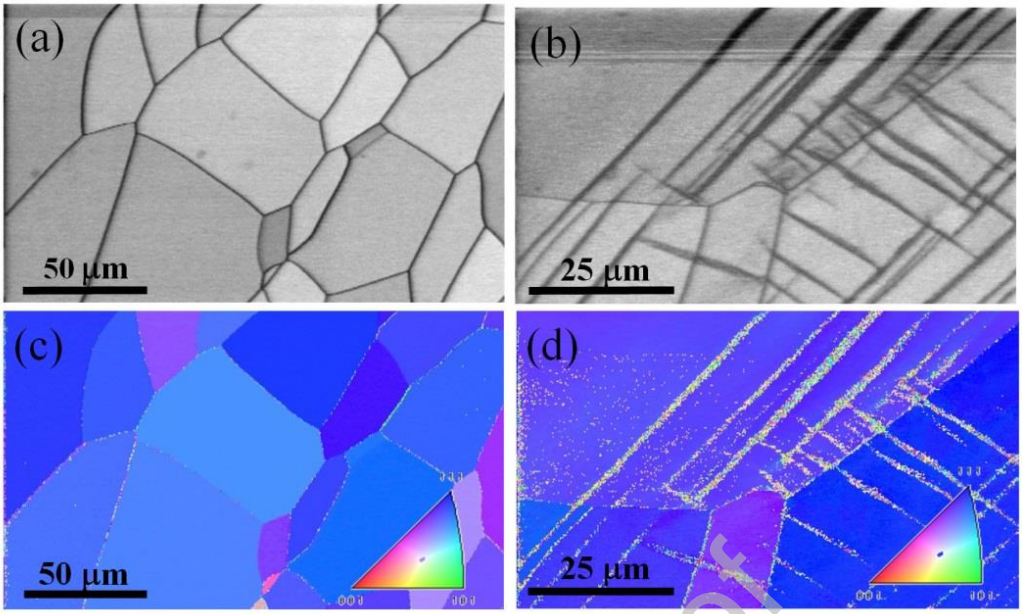

Fig. 4. EBSD image quality (IQ) maps and inverse pole figure (IPF) maps of the normal direction of sample A (a and c) and sample B (b and d); the tensile direction lies along the horizontal direction of all micrographs.

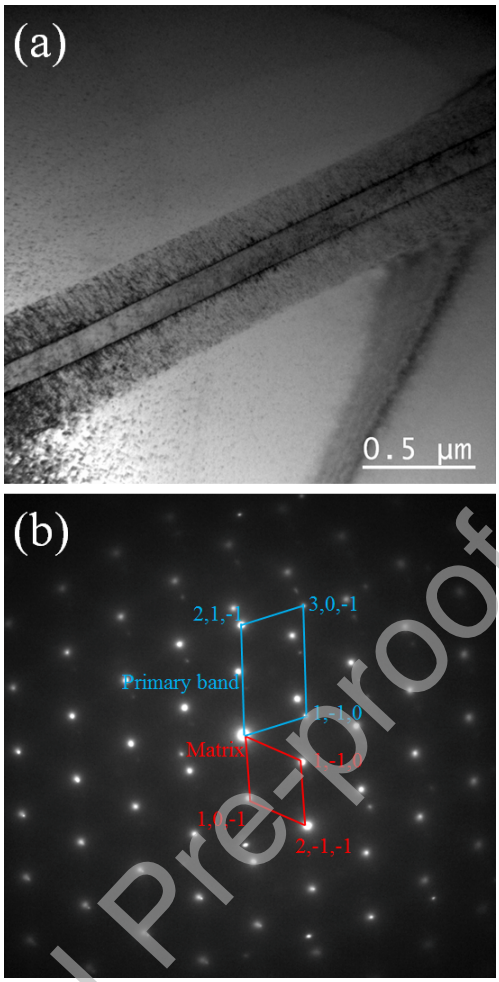

Fig. 5. TEM observations on the sample A: (a) bright field image (BFI) showing a thin deformation band with high density of dislocations at the boundary and (b) the corresponding selected area diffraction (SAED) pattern.

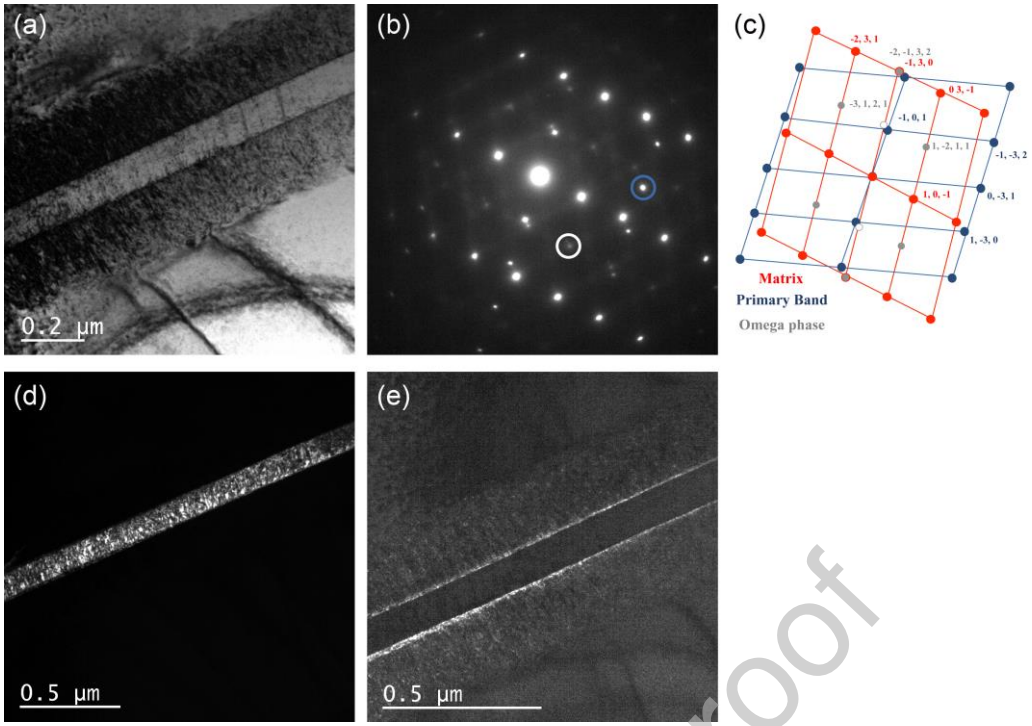

Fig. 6. TEM observations on the sample A under a different diffracting condition: (a) BFI showing the same deformation band with the Fig. 4, (b) the corresponding SAED pattern and (c) its key diagram with white spots corresponding to double diffraction, (d) the DFI of the band highlighted with the diffraction spot marked by blue circle and (e) the DFI of the interfacial omega phase highlighted with a diffused diffraction spot surrounded by white circle.

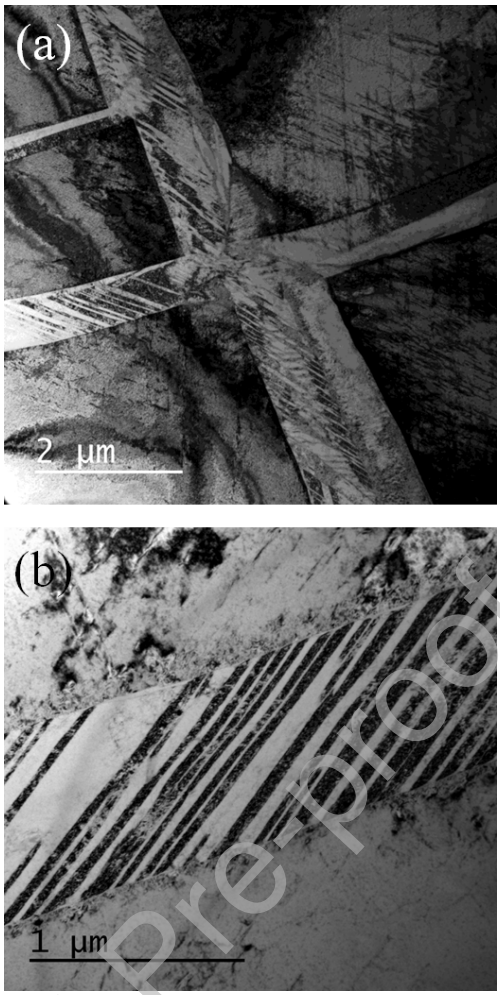

Fig. 7. TEM observations on sample B: (a) a typical deformation microstructure showing some complex deformation bands and (b) details on one single deformation band showing a hierarchical band structure.

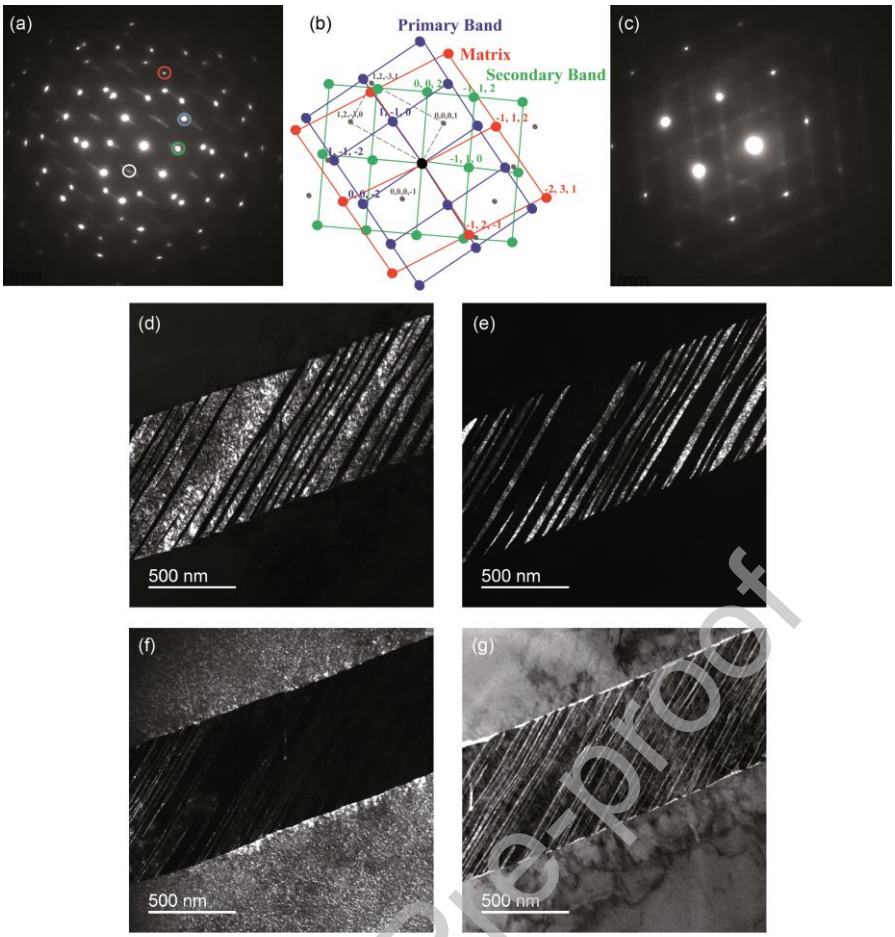

Fig. 8. TEM observations on the sample B: (a) SAED pattern obtained on the edge of the complex deformation band shown in Fig. 7b; (b) key diagram of the SAED pattern with one color for each crystal and ω phase in grey; (c) SAED pattern of the matrix only; (d) (e) (f) and (g) DFIs corresponding to the diffraction spots surrounded inside the SAED pattern by blue, green, red and white circles, respectively.

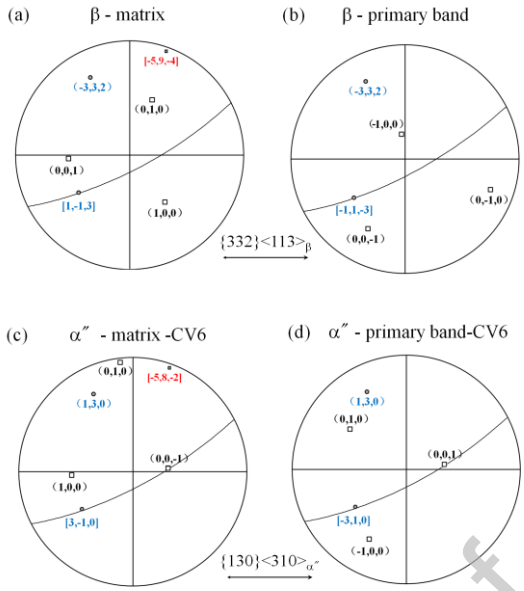

Fig. 9. Crystallographic orientations represented as stereographic for the matrix and the band shown in Fig. 5 for the sample A. The {332}<113> twinning relationship between the β phase matrix (a) and band (b) and the compound {130}<310> twinning relationship between the α″ phase matrix-CV6 (c) and band-CV6 (d) are highlighted.

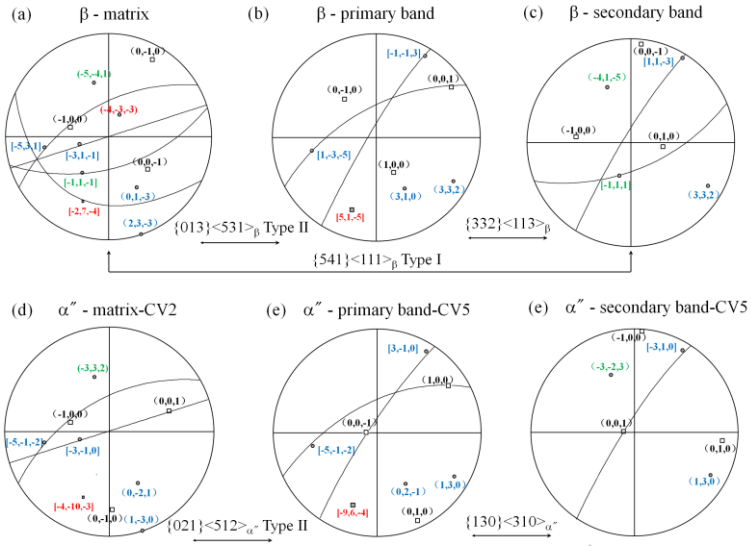

Fig. 10. Crystallographic orientations of the β phase represented as stereographic projections used to determine the orientation relationship (OR) between matrix (a), primary band (b) and secondary band (c) shown in Fig. 8 for the sample B. The corresponding crystallographic orientations of SIM α" phase are represented in (d), (e) and (f).

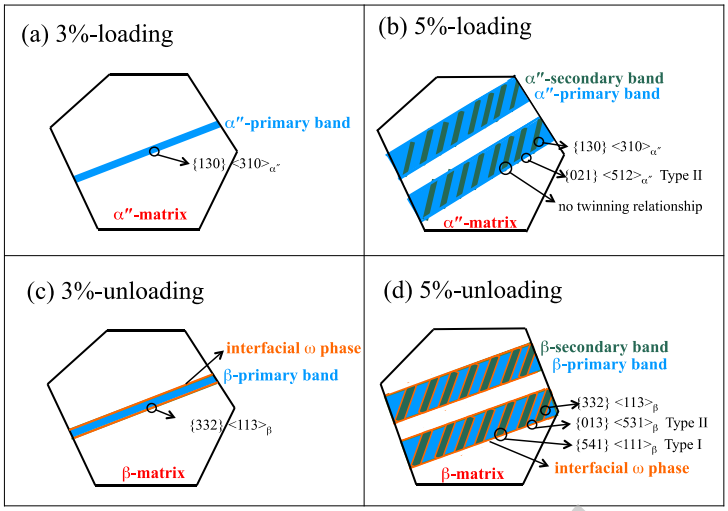

Fig. 11. Schematic illustration of twinning mechanisms occurring during plastic deformation in as-quenched Ti2448 alloy (a-b) and the corresponding relaxed microstructure (c-d).

Table 1. Calculated transformation strains for each correspondence variant of α" martensite (the values of activated variants are in bold underlined)

Variant of α"	**Sample A** (matrix)	**Sample B** (matrix)	**Sample B** (primary band)
CV1	2.45 %	3.69 %	0.02 %
CV2	2.95 %	**4.39 %**	0.18 %
CV3	-1.34 %	-1.81 %	3.97 %
CV4	-1.62 %	-2.00 %	4.81 %
CV5	3.05 %	2.28 %	**0.18 %**
CV6	**3.69 %**	2.63 %	0. 02 %

Table 2. Twinning elements and Schmid factor values of each variant for {332}<113>$_{\beta}$ and {130}<310>$_{\alpha''}$ twinning systems (the values of activated variants are in bold underlined)

Variant number	**K_1**	**η_1**	**SF in Sample A** (between matrix and band)	**SF in Sample B** (between primary and secondary bands)	**SF in Sample B** (between matrix and primary band)
V1	$(332)_{\beta}$	$[11\text{-}3]_{\beta}$	0.03	**<u>0.21</u>**	0.11
V2	$(323)_{\beta}$	$[1\text{-}31]_{\beta}$	0.17	-0.01	0.10
V3	$(233)_{\beta}$	$[\text{-}311]_{\beta}$	0.05	0.05	0.04
V4	$(3\text{-}32)_{\beta}$	$[1\text{-}1\text{-}3]_{\beta}$	0.05	0.05	-0.10
V5	$(3\text{-}23)_{\beta}$	$[131]_{\beta}$	-0.43	-0.01	-0.45
V6	$(2\text{-}33)_{\beta}$	$[\text{-}3\text{-}11]_{\beta}$	-0.05	0.21	0.17
V7	$(\text{-}332)_{\beta}$	$[\text{-}11\text{-}3]_{\beta}$	**<u>0.47</u>**	-0.30	0.37
V8	$(\text{-}323)_{\beta}$	$[\text{-}1\text{-}31]_{\beta}$	-0.29	0.46	-0.17
V9	$(\text{-}233)_{\beta}$	$[311]_{\beta}$	-0.13	-0.30	-0.04
V10	$(33\text{-}2)_{\beta}$	$[113]_{\beta}$	-0.08	-0.32	-0.15
V11	$(32\text{-}3)_{\beta}$	$[1\text{-}3\text{-}1]_{\beta}$	-0.22	0.28	-0.35
V12	$(23\text{-}3)_{\beta}$	$[\text{-}31\text{-}1]_{\beta}$	0.43	-0.32	**<u>0.46</u>**
V1	$(130)_{\alpha''}$	$[\text{-}310]_{\alpha''}$	**<u>0.47</u>**	**<u>0.20</u>**	0.23
V2	$(1\text{-}30)_{\alpha''}$	$[\text{-}3\text{-}10]_{\alpha''}$	0.10	-0.25	**<u>0.46</u>**

Graphical abstract